Adv Polym Sci (2021) 286: 245–272
https://doi.org/10.1007/12_2020_74

Published online: 21 December 2020

Review on the Role of Phase Morphology and Energy Dissipation Around the Crack Tip During Fatigue Crack Propagation of Filler-Reinforced Elastomer Blends

Matthias Wunde and Manfred Klüppel

Contents

Abstract The paper reviews recent investigations of fatigue crack propagation in filler-reinforced elastomer blends based on recipes referring to truck tire tread compounds. One focus lies on viscoelastic energy dissipation effects that explain the well-known power law behavior of the crack growth rate vs. tearing energy. It is demonstrated that the crack growth rate fulfills the time-temperature superposition

M. Wunde and M. Klüppel (✉)
Deutsches Institut für Kautschuktechnologie e.V., Hannover, Germany
e-mail: Manfred.klueppel@DIKautschuk.de

principle by constructing master curves with shifting factors from viscoelastic data. In addition, energy dissipation mechanisms due to stress softening in vicinity of the crack tip are evaluated under quasi-static conditions by calculating the J-integral, which decreases significantly while approaching the crack tip. Therefore, we use combined experimental and theoretical techniques consisting of digital image correlation measurements of the strain field around the crack and calculations of the corresponding energy densities and stress fields based on a physically motivated stress-softening model of filled rubbers. A second focus lies on the role of phase morphology of carbon black (CB) filled NR/BR and NR/SBR blends in fatigue crack propagation. Therefore, the filler distribution is evaluated by an established technique referring to the variation of viscoelastic loss peaks in the glass transition regime. It is found that in NR/BR blends, almost all CB is located in the NR phase, while in NR/SBR blends, the majority of CB is located in the SBR phase. The effect of batching on the phase morphology is also considered, by mixing the NR first with CB and then blending with the second rubber phase. This leads to a more homogeneous distribution of CB in NR/SBR blends. Finally, the obtained fatigue crack growth rates of these blend systems, measured under pulsed harmonic excitations in analogy to rolling tires, are discussed on the basis of the evaluated phase morphology and filler distribution. Here, also the influence of the polymer-filler interphase on the filler distribution is considered.

Keywords Fatigue crack growth · Filled rubber blend · J-Integral · Phase morphology · Tire tread compounds · Viscoelasticity

1 Introduction

Truck tire tread compounds are mostly composed of blends of natural rubber (NR) and butadiene rubber (BR). The most important properties for truck tires are a high wear and abrasion resistance. NR due to its ability to crystallize under strain around the crack tip has the best wear resistance [1]. The crystallization stops cracks very efficiently, which is further improved by the addition of reinforcing fillers [2]. The blending with BR improves abrasion and also rolling resistance. Therefore, blends of NR and BR have a good combination of wear and rolling resistance [3]. However, the blending with SBR can improve wet traction in tires [4]. The role of phase morphology of these mostly phase-separated rubber blends in fracture and wear properties is of high technological interest for improving the overall performance of truck tire tread compounds.

For the fracture and wear of rubber goods, e.g., tire tread compounds, cracks need to be initiated and grow until final failure. Initiation of cracks arises at flaws in the composite, and, therefore, the state of mixing of elastomer compounds is essential for the lifetime of rubber goods. In carbon black filled elastomers, undispersed

agglomerates can act as flaws. Their size is governing the fatigue life, because the propagation rate increases with the size of cracks. Therefore, larger agglomerates may produce larger initial cracks which will reduce the lifetime of rubber goods significantly [5, 6]. However, when studying fracture mechanics of elastomers, the main focus is on the propagation of existing cracks in the rubber matrix. It specifies how rapidly a crack is growing under different loading conditions. The basics of fracture mechanics started with Griffith's work on glassy material [7], but after the Second World War, it was mainly developed on metals and later applied to all kind of materials [8]. For elastomers the tear resistance determined during growth of existing cracks is strongly increased by active fillers and by strain-induced crystallization [4, 9]. The improvement of crack growth resistance due to the filler increases with decreasing carbon black particle size [10]. For unfilled non-crystallizing elastomers, the crack growth behavior is inferior and depends more on the type of cross-links than on the polymeric structure [11]. The energy needed to increase the crack length of an elastomer sample is in general higher than the energy to break the respective polymer bonds in the freshly created crack surfaces. The energy to break the bonds is connected to the intrinsic strength, T_0 [70]. The difference between the energy necessary to break the sample and the energy to break the bonds can be attributed to energy dissipation around the crack tip. A linear viscoelastic theory of steady crack propagation was formulated for unfilled elastomers, which refers to the energy dissipation during the glass transition of the rubber [12–14]. It is not clear in how far similar concepts can be used for the description of fatigue crack growth (FCG) of filled elastomers, though the phenomenology appears very similar.

In the present review, we will briefly review basic theories regarding crack growth in viscoelastic materials and report about viscoelastic fingerprints during fatigue crack growth of elastomers by applying the time-temperature superposition principle. In addition, the dissipated energy around the crack tip of various filled rubber blends, with formulations close to truck tire tread compounds, is evaluated under quasi-static conditions by combining digital image correlation (DIC) measurements with the J-integral method. As a result a spatial resolution of the local energy dissipation due to stress-softening effects will be obtained. Further studies are related to various effects of blending of NR with SBR and BR, as typically used for truck tire treads, on fatigue crack propagation rates. Therefore, the phase morphology and the distribution of CB on the different phases are investigated.

2 Basic Concepts of Fracture Mechanics

2.1 Griffith Criterion

A crack in a solid does not grow by itself. To increase the crack from crack length c to $c + dc$, energy must be used to break the atomic bonds at the newly formed crack surface, $A = 2\, dc \cdot t$ (Fig. 1). The crack length, c, is given as the half contour length

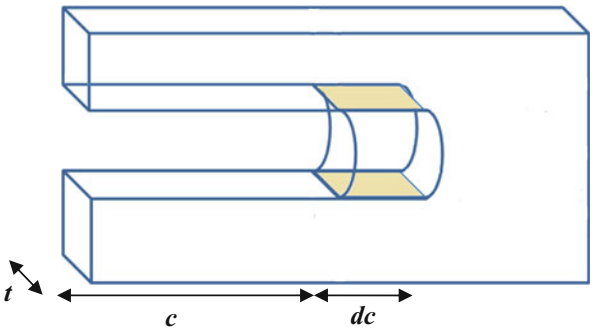

Fig. 1 Schematic drawing of a crack growing from length, c, to length, $c + dc$. The newly formed crack surfaces are shown as colored surfaces

of the crack. Therefore the surface energy, $dS = 2\ dc \cdot t \cdot \gamma_0$, is necessary to grow the crack. Here, t is the thickness of the sample and, γ_0 is the specific surface energy.

When a sample is being deformed, elastic strain energy, W, is stored. If a crack is growing, the deformed material is partially relieved, and some part of the elastic strain energy is released. According to the Griffith criterion, a crack is growing when the surface energy of the newly created surface, dS, is (over)compensated by the released elastic strain energy, $-dW$:

$$-\frac{dW}{dc} \geq \frac{dS}{dc} \tag{1}$$

Griffith calculated the released strain energy for an infinite half plate in uniaxial tension. Comparison of the surface energy increase with the elastic strain energy decrease yields growth for cracks exceeding a critical length, c^* [7].

2.2 *Evaluation of Tearing Energy for Different Sample Geometries*

The tearing energy, $T = -(dW/dS)_t$, denotes the characteristic energy of a material which is necessary to increase the length of a crack. If a crack is growing depends not directly on the sample geometry or the forces which are applied at the specimen borders far away from the crack tip. Important for the crack growth is the state of deformation close to the crack tip. The state of deformation is determined by the shape of the cut and the strain at the crack tip. The tearing energy for a single-edge notched tensile sample (SENT-Sample), which is deformed uniaxially, is given by [15]

$$T = \frac{2\pi}{\sqrt{\lambda}} W_{el} c \tag{2}$$

Here, λ is the strain, W_{el} is the elastic energy density far away from the crack tip, and c is the half crack contour length of the crack. The tearing energy is calculated

from the energy difference, dW, between the notched sample in comparison to the unnotched one. The $\sqrt{\lambda}$-term in the denominator was added by Clapson and Lake [16] to account for the transversal contraction of rubber at larger strain, which follows from the constant volume assumption and can be described by a Poisson's ratio, $\mu = -\ln(\lambda_2)/\ln(\lambda_1) = 0.5$. Unfilled natural rubber has a Poisson's ratio of nearly 0.5, but it is decreasing with carbon black content [17]. The Poisson's ratio is also decreasing at large strains, low temperatures, and short measurement times [18]. The decrease follows time-temperature superposition and is associated with the transition of the rubber into the glassy state [18]. Although for different sample geometries distinct formulas for the tearing energy are used, it is a material specific quantity. This has been shown by comparing the crack growth velocities of different materials [19].

When the sample is strained in one direction and the deformation in a second direction is prevented, the sample can only contract in the third direction. This is the case for the plane strain (PS) tension samples. For a sufficient long PS sample, two states, which differ only in their crack length, c, and, $c + dc$, simply differ in a volume, $ht\,dc$, being before and after the crack tip, respectively. Here, h and t are the height and the thickness of the undeformed sample, respectively. This yields a difference in strain energy, $dW = -W_{el}ht\,dc$. The tearing energy of PS samples is then

$$T = W_{el}h \tag{3}$$

Contrary to the SEN-Samples, the tearing energy for PS samples is thus independent of crack contour length c.

2.3 The J-Integral

The tearing energy considered in Sect. 2.2 is representing the global value of the energy available for surface growth of the propagating crack. In contrast, the concept of the J-integral introduced by Cherepanov and Rice [20, 21] delivers a local value of the tearing energy that may depend on the distance to the crack tip.

The J-integral is based on a path integral taking into account the 1. Piola-Kirchhoff stress tensor, P; the elastic energy density, W_{el}; and the displacement gradient, $H = (\partial U_i/\partial x_j)_{ij}$, with the element in the i-th row and the j-th column given by $\partial U_i/\partial x_j$, along a contour, Γ, around the crack tip (see Fig. 2). The first component of the J-integral, J_1, describes the local value for the tearing energy regarding straight crack propagation:

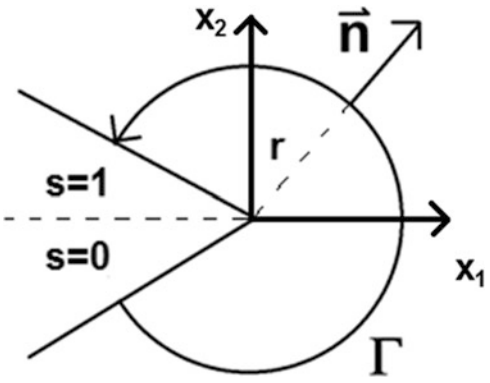

Fig. 2 Integration path $\Gamma(s)$ of the J-integral around the crack tip

$$J_1 = \oint_{\Gamma} \left[W_{el} N_1 - P_{ij} N_j \frac{\partial U_i}{\partial X_1} \right] d\Gamma \tag{4}$$

Here, $U = x\text{-}X$ is the displacement vector giving the difference between the deformed coordinates, x, and the undeformed coordinates, X. $F = I + H$ is the deformation gradient, and I is the unity matrix. The 1. Piola-Kirchhoff stress tensor is given by $P = \det(F)\sigma(F^T)^{-1}$ [22]. F^T is the transpose of the deformation gradient, F. Assuming incompressibility of the rubber leads to $\det(F)=1$. For small deformations the 1. Piola-Kirchhoff stress converges into the Cauchy stress σ. The J-integral can be described in the framework of material forces [23] with the integrand of the J-integral given by the Eshelby stress tensor [24].

For purely elastic materials, the J-integral over a closed path not containing voids or cracks is zero. In that case the J-integral surrounding the crack tip is path-independent. The only sink of the energy flux is then the crack tip. In filled elastomers also significant energy dissipation occurs far away from the crack tip due to strong nonlinearity and hysteresis. The J-integral can then capture the energy that is flowing into a small volume around the crack tip. In this region the energy is available for surface growth of the propagating crack [25, 26].

The J-integral is strictly only applicable on stationary cracks, but the concept can be generalized to growing cracks [25, 27]. One difference is that then the kinetic energy density is added to the elastic energy density, W_{el}, to build the total mechanical energy density. For nearly stationary conditions with very slowly moving cracks, the kinetic energy density is very small and can be neglected. Freund [25] examined the energy flow into a body in the x_1, x_2, t-space, in which the time, t, is regarded as additional dimension and determined the instantaneous rate of energy flow, $F(\Gamma)$, through the integration path, Γ, which both $F(\Gamma)$ and Γ depend on the instantaneous crack tip velocity, v_c. When the fields of all state variables within the contour, Γ, translate invariant with the moving crack, this so-called energy flux integral can be written as $F(\Gamma) = J \cdot v_c$.

2.4 Fatigue Crack Growth of Elastomers

In fatigue crack growth experiments, a notched sample is loaded cyclically. The excitation can be harmonic or pulsed. The crack growth is measured as crack growth, *dc*, per loading cycle, *n*. Also, for dynamic crack growth, the crack growth rate, *dc/dn*, of a crack in a material depends only on the tearing energy, *T*, and not on the sample geometry [28]. In dependence on tearing energy, three different crack growth regions can be distinguished: (1) Below the intrinsic strength, T_0, nearly vanishing crack propagation takes place. The crack growth rate, *dc/dn*, in this region is very low ($\lesssim 10^{-8}$ mm/cycle) and independent of the tearing energy but depends on the ozone concentration. The intrinsic strength, T_0, has recently been measured to 0.051 N/mm and 0.100 N/mm for NR and BR, respectively [29]. This energy values are in the order of magnitude to break the chain bonds and just above T_0, the crack growth rate increases linearly [30]. (2) In a range of intermediate tearing energies, *T*, the crack growth rate, *dc/dn*, follows a power law. This dependency is called Paris-Erdogan law [31, 32]:

$$\frac{dc}{dn} = AT^B \tag{5}$$

The log-log plot of *dc/dn* in dependence of *T* is the fatigue crack growth characteristic. In this plot the prefactor, *A*, is given as axis intercept, and the exponent *B* determines the slope. (3) Above a critical tearing energy, T_c, catastrophic tearing takes place, and the crack growth rate, *dc/dn*, becomes extremely large. The critical tearing energy, T_c, is around 100–1,000 times higher than the intrinsic strength, T_0 [28, 30]. In viscoelastic crack growth theories, the ratio between T_c and T_0 corresponds to E'_∞/E'_0, the ratio between the storage moduli at infinite, E'_∞, and zero frequency, E'_0.

2.5 Crack Propagation in Viscoelastic Solids

The stress intensity factors *K* describe the stress state at the crack tip. They depend on the loading as well as on the geometry of crack and sample. For linear (visco)elastic, homogeneous, and isotropic materials, the stress field under plane stress conditions fulfills the universal relation $\sigma(r) \cong K/\sqrt{r}$ with the distance, *r*, from the crack tip [33]. The displacement field, $u(r)$, is obtained from $\sigma(r) = E\frac{d}{dr}u(r)$ as $u(r)(\tilde{K/E})\sqrt{r}$ yielding for the tearing energy, $T = K2/E \cong \sigma\ u$, independent of *r*. The Young's modulus $E = \sigma/\varepsilon$ describes the resistance of a material to uniaxial stress, σ, at a small strain, ε.

2.5.1 Viscoelastic Crack Opening Mechanisms in Soft Adhesives

De Gennes [34] introduced the concept of crack opening mechanisms in soft adhesives to calculate the tearing energy of a simple viscoelastic solid with the frequency-dependent tensile modulus, $E^* = E_0 + (E_\infty - E_0)i\omega\tau/(1 + i\omega\tau)$. Here, ω and τ are the angular frequency and the relaxation time, respectively, and i is the unit imaginary number of the complex numbers. E^* reflects the terminal flow regime of a very slightly cross-linked (monodisperse) polymer melt just above the gel point which is often used for soft adhesives. Then the relaxation time, τ, can be identified with the reptation time of the chains which strongly varies with the molar mass, M, as $\tau_{rep} \sim M^{3.4}$ and hence can be adjusted to practical demands by moving the time scale. The real and imaginary parts of the modulus, E' and E'', respectively, of a simple viscoelastic solid are depicted in Fig. 3a. The related velocity-dependent tearing energy is shown schematically in Fig. 3b. Three regimes can be distinguished: For small or large frequencies, the system behaves like a soft or hard solid, respectively, since $E' >> E''$. The tearing energy differs and is given by $T_c = K2/E_0 \cong \sigma\, u$ for the soft solid regime and $T_0 = K2/E_\infty \cong \sigma\, u$ for the hard solid regime. Since the strain rate $\frac{d}{dt}\frac{d}{dr}u(r)\tilde{1}/\sqrt{r}$ increases significantly while approaching the crack tip, the hard solid regime is found in the vicinity of the crack tip while the soft regime is found in the outer region far away from the crack tip, provided the crack velocity is sufficiently high. In the intermediate frequency regime $\frac{E_0}{E_\infty \tau} < \omega < \frac{1}{\tau}$, the system can be approximated by a liquid with viscosity $\eta = (E_\infty - E_0)\tau \cong E_\infty \tau$ because $E' < E''$ (see Fig. 3a). The stress field is then related to the displacement field by the equation $\sigma = \eta \frac{d}{dr}\frac{du}{dt} = \eta v \frac{d^2}{dr^2}u$ which is solved by $u(r) \cong (K/v\tau E_\infty)r^{3/2}$ with v being the stationary crack velocity. Accordingly, the tearing energy increases linearly with the distance, r, from the crack tip: $T \cong \sigma u \cong \frac{K^2 r}{v\tau E_\infty} \cong \frac{r}{v\tau}T_0$ [34]. For $r \leq v\tau$ it takes the constant value, T_0, of the hard solid close to the crack tip, and for $r \geq (E_\infty/E_0)v\tau$, it takes the much larger value, T_c.

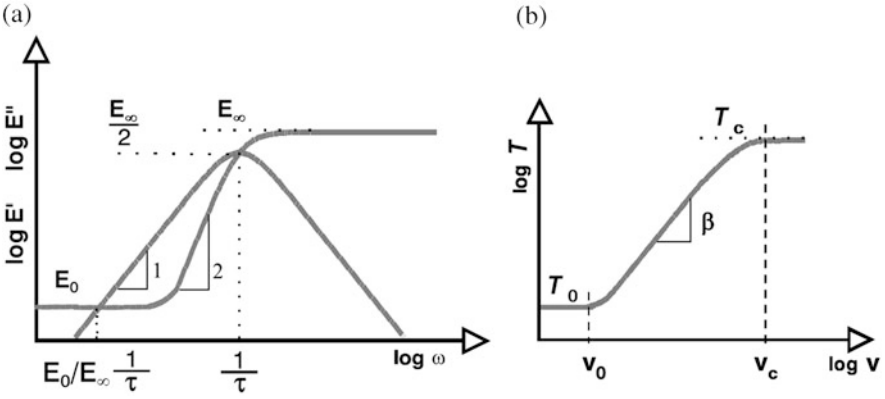

Fig. 3 Storage and loss moduli of a linear viscoelastic solid (**a**) and related velocity-dependent tearing energy (**b**)

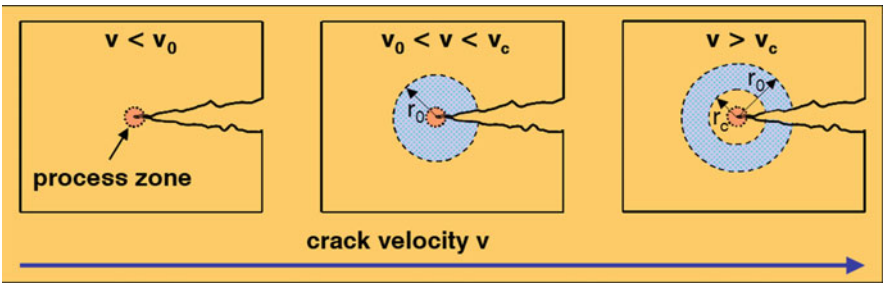

Fig. 4 Viscoelastic crack opening mechanism close to the crack tip. The blue shaded area corresponds to the regions with high energy dissipation

This indicates that for sufficient large crack velocities, when the region close to the crack tip behaves like a hard solid, only a small part of the tearing energy given by E_0/E_∞ is available at the crack tip since most of the energy is dissipated in the transition zone of the viscoelastic solid. Then, the crack contour takes a trumpetlike shape which is created as in both the soft solid regime far away from the crack tip and the hard solid regime in the vicinity of the crack tip, where the displacement, $u(r)$, is increasing proportional to $\sqrt{r}$, but in the transition regime, the displacement is varying with $r^{3/2}$ [34]. Energy dissipation around the crack tip can be neglected only for sufficient small crack velocities, $v < v_0$, where $T = T_0$. The onset of energy dissipation for soft adhesives can be evaluated as $v_0 \cong a\,(E_0/E_\infty)/\tau_{rep}$ with a being a nanoscopic length scale where chain disentanglement takes place. For $v > v_0$ the tearing energy increases linearly implying $\beta = 1$ for the exponent in Fig. 3b. For $v > v_c \cong a/\tau_{rep}$ the tearing energy reaches the final plateau value $T_c = (E_\infty/E_0)T_0$. This velocity dependence of the tearing energy is depicted in Fig. 3b. The evolution of the dissipation regime around the crack in dependence of crack velocity, v, is shown schematically in Fig. 4.

2.5.2 Viscoelastic Crack Growth in Rubber

Crack propagation in cured rubbers shows a very similar behavior as for soft adhesives though the terminal flow regime depicted in Fig. 3a disappears with increasing cross-link density. It is replaced by a rubber elastic plateau, which shows little energy dissipation. However, another relaxation transition is found at higher frequencies, the rubber-glass transition, which affects crack propagation in a similar way. The rubber-glass transition is related to a Rouse-like relaxation of the polymer strands between adjacent chain entanglements implying that the onset of energy dissipation is determined by the Rouse relaxation time, τ_{Rouse} , which scales with the square of the entanglement molar mass of the rubber, $\tau_{Rouse} \sim M_e^{\,2}$ [35]. A linear viscoelastic theory of propagating cracks in rubber was developed by Persson and Brener, which refers to the full relaxation time spectrum of the rubber in the glass transition regime [12]. The important point is that the deformation rate

compared to the bulk is significantly increasing when approaching the crack tip. Therefore, closer to the crack tip and with increasing crack velocity, v, the excitation frequency rises strongly so that the elastomer is behaving more and more glassy. This leads to a significant increase of energy dissipation around the crack tip as depicted schematically by the blue shaded area in Fig. 4. The size of the dissipation regime is determined by the two radii, $r_0 \cong v\,\tau_{\text{Rouse}}$ and $r_c \cong \left(E'_\infty/E'_0\right)^{1/\beta} v\,\tau_{\text{Rouse}}$.

The velocity dependence of the tearing energy depicted in Fig. 3b can be expressed semiempirically as [36, 37]

$$T = T_0\left(1 + \frac{E'_\infty/E'_0}{(1 + v_c/v)^\beta}\right) \tag{6}$$

Here, E'_∞ and E'_0 are the real parts of the tensile moduli in the glassy and rubbery regime, respectively, and $v_c \cong v_0\left(E'_\infty/E'_0\right)^{1/\beta}$ is the critical crack velocity where the tearing energy reaches a plateau value, $T_c \cong (E'_\infty/E'_0)T_0$, where the crack tip is behaving glassy and catastrophic crack growth takes place. For low crack growth velocities, $v < v_0$, the tearing energy, T, is given by the intrinsic strength, T_0, which is the threshold value below which no fracture occurs. It is connected to the fracture in the crack tip process zone, which is a complex region of nanoscopic size, a, where bond fracture, chain pullout, and cavity formation appear (see Fig. 4). The onset of energy dissipation can be evaluated as $v_0 \cong a/\tau_{\text{Rouse}}$. For higher crack growth velocities $v_0 < v < v_c$, the tearing energy follows a power law, $T \sim v^\beta$. The exponent β was shown to be related to the exponent, m, of the relaxation time spectrum, $H(\tau)$, in the glass transition regime [12]. This can be determined from the course of the storage modulus, E', (given by its smoothed master curve) using, e.g., the approximation method of Ferry and Williams [38]. The exponent, m, can be used to predict the exponent, $\beta = (1 - m)/(2 - m)$, of the power law increase of the tearing energy with crack velocity, v [12].

The exponent $\beta^{-1} = (2 - m)/(1 - m)$ obtained from the relaxation time spectrum for steady crack growth with constant crack velocity roughly coincides with the exponent, B, of the power law in the FCG characteristic (Paris-Erdogan law) (Eq. (5)) [36]. This indicates that viscoelastic crack opening mechanisms play also a role in FCG experiments explaining the Paris-Erdogan power law behavior (Eq. (5)). The exponent, m, in filled compounds decreases with filler loading and strength of polymer-filler interaction, predicting smaller exponents, B, with filler loading and activity, in agreement with experimental data [36]. Equation (6) was also used for a semiempirical description of the shear stress in adhesion friction that has the same velocity dependency [37]. The critical velocity, v_c, increases systematically with decreasing glass transition temperature [39], and an equivalent increase of v_c with increasing sample temperature is found. This correlates with the measured adhesion friction very well.

The viscoelastic nature of FCG in rubber becomes also apparent when measurements at different temperatures are compared, indicating that the time-temperature superposition principle is fulfilled. Figure 5a shows results of fatigue crack

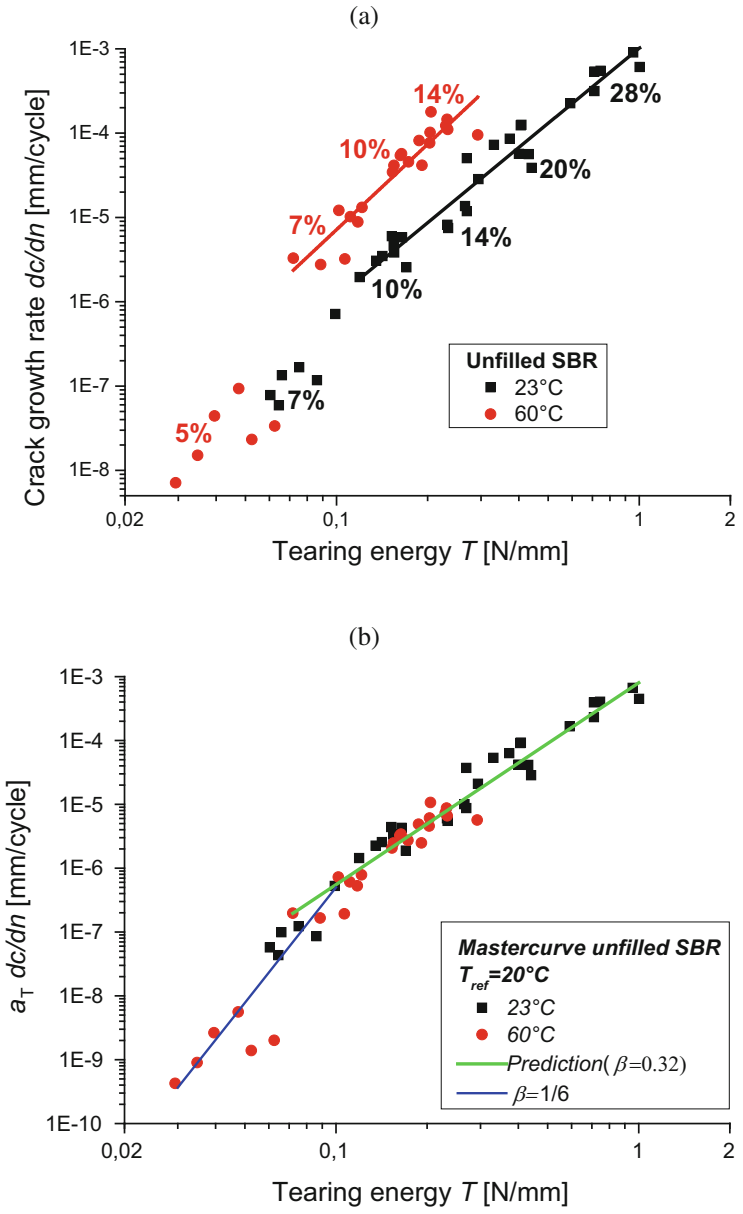

Fig. 5 Fatigue crack growth rate *dc/dn* vs. tearing energy *T* (FCG characteristics) for unfilled SBR at 23°C and 60°C (**a**) and master curve obtained by multiplying the crack growth rate *dc/dn* with the horizontal shifting factors a_T (**b**). The preload is 0.09 MPa (2 N) (from [40])

propagation of unfilled SBR with SEN-Samples at two different temperatures, 23 and 60°C [40]. The tearing energy for the cyclic tearing of unfilled SBR is calculated with Eq. (2). The (harmonic) excitation rate is low (2.5 Hz) to avoid flash temperature effects, which denotes the increased temperature close to the crack tip due to energy dissipation. Obviously, the propagation rate is about one decade smaller for measurement at 23°C. This correlates with the observation that fatigue life in unfilled SBR increases by a factor of about 10^4 when the temperature decreases from 100°C to 0°C [41, 42]. Using the WLF equation with the parameter obtained from viscoelastic master curves for the dynamic moduli, a master curve for the tearing energy in steady tearing can be established [43, 44]. The master curve in Fig. 5b demonstrates that this is also possible for fatigue crack growth. For higher tearing energies, the master curve follows a power law with exponent, $B = \beta^{-1}$, with the exponent, $\beta = (1 - m)/(2 - m) = 0.32$, obtained from the exponent, $m = 0.54$, of the relaxation time spectrum [40].

Creating master curves is possible also for filled compounds. However, in the calculation of tearing energy, a master curve is only achieved if the dynamic part of the energy density is used [40]. The dynamic energy density is the integral $\int \sigma_{dyn} d\varepsilon$, with σ_{dyn} being the dynamic energy density that neglects the preload. For both the unfilled and the filled compounds, two distinct slopes are found at high and low crack growth rates. Two distinct slopes were also reported by M. Ludwig who demonstrated that the higher slope at lower tearing energies should be used for lifetime predictions [45].

3 Experimental

3.1 Sample Preparation

The composites used in this study are polymer blends of natural rubber (SVR CV 60) blended with butadiene rubber or styrene butadiene rubber with varying proportion of the polymers and filled with 50 phr carbon black (N339). The butadiene rubber (BR) used is a high-cis butadiene rubber (Buna CB 24, Arlanxeo), and the styrene-butadiene rubber (SBR) is a solution styrene-butadiene rubber (Buna VSL 4526–0 HM, Arlanxeo) with 45 wt.% vinyl and 26 wt.% styrene groups. Neither the rubbers nor the compounds contain oil. The samples are cross-linked semi-efficiently by sulfur together with the vulcanization accelerator N-cyclohexyl-2-benzothiazole sulfenamide (CBS). The samples are compounded with the processing and vulcanization additives stearic acid and ZnO and protected against aging by N-isopropyl-N-phenyl-P-phenylenediamine (IPPD). The full recipe is shown in Table 1.

The compounds are mixed in an industrial 5 L intermeshing mixer (Werner & Pfleiderer GK 5 E) at 40 rpm for 6 min. Two different mixing techniques are used. In the standard mixing procedure, the other ingredients are inserted after 2 min mastication of the polymers. In the batching mixing procedure, the filler is blended with

Table 1 Recipe of filled rubber blends. The compounds marked with * are additionally produced with the batching mixing procedure (carbon black blended first in NR only)

Compound	NR	BR	SBR	CB	CBS	Sulfur	IPPD	ZnO	Stearic acid
N85B15	85	15	–	50	2.5	1.7	1.5	3	1
N70B30*	70	30	–	50	2.5	1.7	1.5	3	1
N55B45*	55	45	–	50	2.5	1.7	1.5	3	1
N85S15	85	–	15	50	2.5	1.7	1.5	3	1
N70S30*	70	–	30	50	2.5	1.7	1.5	3	1
N55S45*	55	–	45	50	2.5	1.7	1.5	3	1
N70B15S15*	70	15	15	50	2.5	1.7	1.5	3	1
N55B23S23	55	22.5	22.5	50	2.5	1.7	1.5	3	1

the NR only. The BR and the other ingredients are added in a second mixing stage. Leveling of the torque after mastication and after mixing indicates homogeneous mixtures. The curing system is added on a roller mill, where the compounds are handled another 7 min. Vulcanization is performed at 150°C in a heat press up to 90% of the vulcameter torque maximum (t_{90} time). The carbon black dispersion, as measured by optical dispersion analysis, is larger than 90% for all compounds.

3.2 Dynamic Mechanical Analysis

The dynamic mechanical measurements are performed in the torsion rectangular mode with strip specimen of 2 mm thickness on the dynamic analyzer ARES (Rheometrix). The dynamic moduli are measured over a wide temperature range (−115°C to +20°C) at frequency of 1 Hz and 0.5% strain amplitude. The compounds are measured after a quick cool down while heating. In the heating process, the chamber temperature is increased successively by 1°C.

3.3 Fatigue Crack Growth Analysis

The fatigue crack growth is measured at single-edge notched tensile sample (SENT-Sample) on a Tear and Fatigue Analyzer (Coesfeld GmbH & Co. KG, Germany). This machine allows a fully automatic detection of crack length for investigating ten specimens simultaneously. The crack propagation rates are measured under pulsed excitation (4 Hz, 30 ms pulse width, waveform = Gaussian pulse) at 60°C. The 15 mm broad samples with a 1 mm notch are pre-strained by 2 N and excited by varying strain amplitudes (normally between 10% and 30%). The graphical images for determination of the crack length are triggered between the pulses.

3.4 Digital Image Correlation Analysis

The displacement fields are measured by photogrammetric techniques using the digital image correlation (DIC) software ARAMIS from GOM, Germany. A fine black and white pattern is created by airbrushing the samples gently with white paint (Faskolor from Parma International). The change of the pattern when the samples are deformed is calculated into the evolution of the displacement field. The stretching of the composites is performed in a Zwick universal testing machine 1,445 at a speed of 20 mm/min. The notched PS samples are strained five times to the same maximum strain value varying between 10% and 60%. A high-speed camera is used, but only one image per second of the last deformation cycle is recorded. The spot size is approximately 20 mm $\times$ 20 mm, and the resolution is around 1000 $\times$ 1000 pixel. The image at the start of the cycle showing the smallest deformation is taken as reference configuration. Only the displacement field of the image with the highest deformation is used for evaluation. Due to the limited rate of one image per second, both the reference image and the evaluated images do not exactly correspond to the lowest and highest strains during the cycle, respectively.

4 Effect of Stress Softening on Energy Dissipation as Evaluated by the J-Integral

The J-integral allows for the consideration of energy dissipation mechanisms around the crack tip that lower the available energy for crack growth. In this section the effect of energy dissipation due to stress softening of the filled rubber blends on the available energy for crack propagation is investigated [46]. For the evaluation of the J-integral, the deformation fields around the crack tip of stretched samples have been measured by DIC. The corresponding energy and stress fields are calculated by using a recently developed model of stress softening of filled rubbers [47]. In this model the energy density is separated into two parts, an elastic part and a hysteretic part. The J-integral is evaluated at the end of the cycle, where the hysteretic contribution vanishes. The critical stress parameter σ_c of the model is set to zero. The elastic part is based on the behavior of the unfilled elastomer matrix given by the extended non-affine tube model [48], but including hydrodynamic reinforcement of the filler. The hydrodynamic reinforcement is implemented via an amplification factor X, which describes the overstretching of the elastomer due to presence and rigidity of the filler. The elastic energy density is calculated as integration of the energy density from the extended non-affine tube model multiplicated by a distribution, $P_X(X) \sim X^{-\chi}$, of amplification factors. To identify the parameters of the physically based model, multihysteresis measurements on dumbbell samples have been performed. The obtained parameters are the cross-linking modulus, G_c; the entanglement modulus, G_e; and the average number of statistical segments between trapped entanglements,

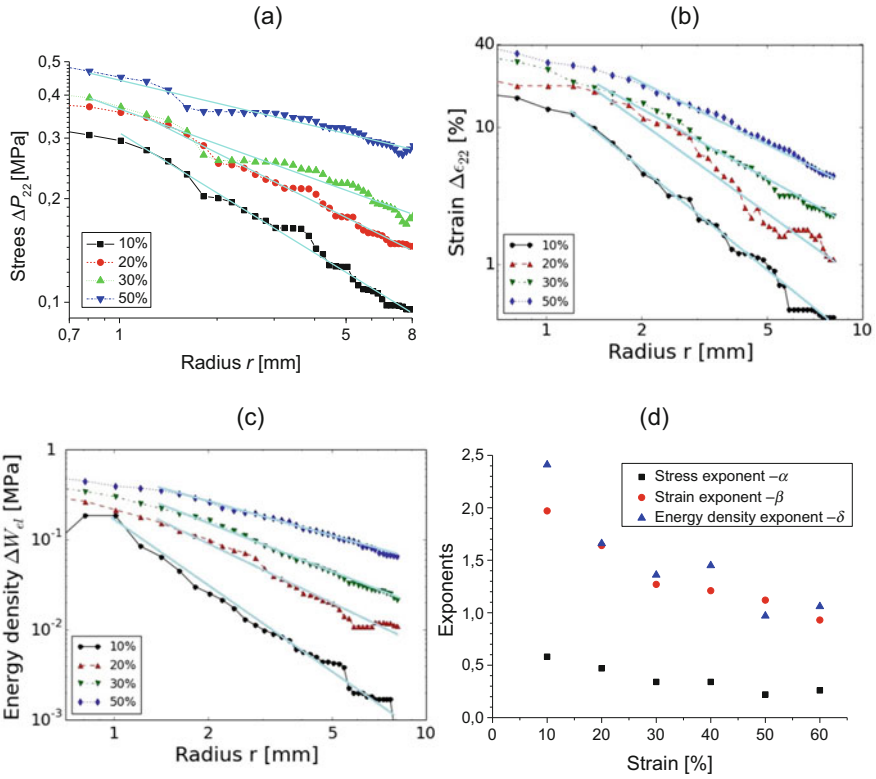

Fig. 6 Log-log plots of the stress increase $\Delta P_{22} = P_{22} - P_{\infty}$ (**a**), strain increase $\Delta\varepsilon_{22} = \varepsilon_{22} - \varepsilon_{\infty}$ (**b**), and energy density increase $\Delta W_{el} = W_{el} - W_{\infty}$ (**c**) when approaching the crack tip at $X_2 = 0$ for different strain levels, as indicated. The straight lines correspond to power law behavior with varying distance r from the crack tip. The exponents for different strains are depicted in (**d**) (from [46])

n. The filler network is characterized by the effective filler volume fraction, ϕ_{eff}; the cluster extensibility parameter, γ; and the power law exponent, χ.

Figure 6 shows results obtained for stress, strain, and energy density around the crack tip of a PS sample, which all show a power law decline toward the values far away from the crack tip. The exponents clearly differ from the exponents expected from linear elastic fracture mechanics [8]. At small strain values, the obtained exponents for strain are almost four times larger than the elastic reference value (-0.5). This indicates a stronger singular behavior due to strong stress-softening effects. At higher strain amplitudes, this is less pronounced since the level of strain is larger far away from the crack tip. This implies that less stress softening appears when approaching the crack tip. The singular behavior can only be analyzed as long the deformations can be recorded reasonably.

The J-integral Eq. (5) considers the integration on a path Γ around the crack tip over an integrand which consists of a sum of two contributions. Both contributions

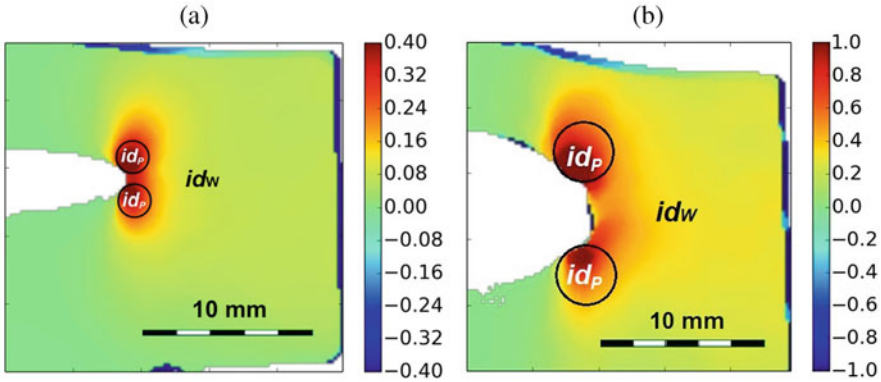

Fig. 7 Integrand of the J-integral J_I for the NR composite elongated by 20% (**a**) and 50% (**b**). The areas where the respective components id_W and id_P are dominating are indicated. J_I is calculated by Eq. (5) as integral around circular paths Γ (from [46])

depend on the integration path and the normal vector of this path. One contribution, denoted id_W, only depends on the energy density distribution. The other contribution, denoted id_P, depends on the 1. Piola-Kirchhoff stress tensor and the displacement gradients. By choosing a circular contour for Γ, the two different contributions can be visualized. The separation of the integrand yields that far away from the crack tip, the field is dominated by id_W, but close to the crack tip, id_P gives the largest contributions to the crack tip in both lateral directions. The integrand of the J-integral J_I and its distribution on id_W and id_P is shown as color code in Fig. 7 for the NR composite elongated by 20% and 50%, respectively.

The J-integral has been determined for four selected compounds and for different strain levels in dependence of the distance from the crack tip. The results are shown in Fig. 8. The J-integral is known to be path-independent for purely elastic materials. In Fig. 8 it is found to increase significantly for circular paths around the crack tip with increasing size r until a plateau is reached. The data indicate that more than 90% of the elastic energy is not available for crack growth since it is dissipated in the stress-softening area around the crack tip. For smaller strain amplitudes, the plateau value of J_I coincides with the global tearing energy T evaluated with Eq. (3). For strain amplitudes larger than 40%, the plateau value of J_I is found systematically larger than the global tearing energy T for all compounds.

5 Influence of Blend Morphology on Fatigue Crack Growth

The fatigue crack growth behavior of filled elastomer blends under specified loading conditions depends not only on the polymers and fillers used, and their respective amounts in the compound, but also on the influence of blend morphology and filler distribution. The influence of these morphological aspects on the crack propagation

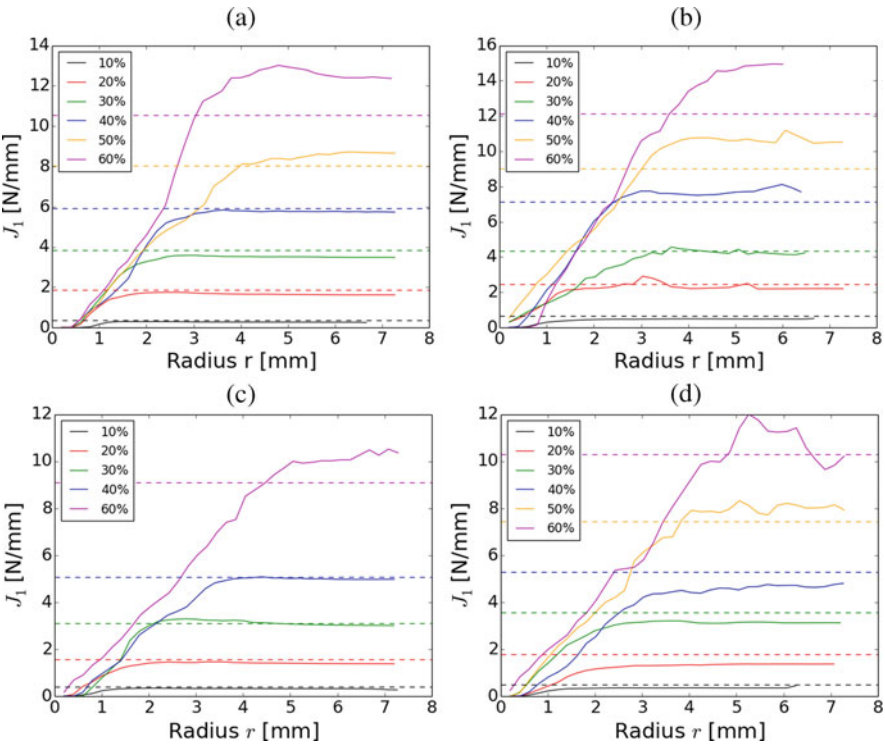

Fig. 8 J_1 for strain amplitudes between 10% and 60% for the NR composite (**a**), N55B45 (**b**), N55S45 (**c**), and N55BS23 (**d**). The global tearing energy $T = W_\infty h$ for different strain amplitudes is shown as dashed lines for comparison (from [46])

rate of blends measured by the tear fatigue analyzer has been analyzed for the compounds listed in Table 1 [49, 50]. For the blend systems marked by a star, the compounds have been mixed in two different ways: the standard mixing procedure in which the filler is added to the premixed blend and the batch mixing procedure in which the filler is added to the pure NR and then blended with the other rubbers.

5.1 Evaluation of Phase Morphology

The method used to determine the phase morphology and filler distribution in these blends relies on the increase of peak heights of the loss shear modulus, G'', due to the filler incorporated into the respective polymer phases and on the additivity of dissipated energies, whereby the dissipated energy in the blend is given by the sum of the dissipated energy in the different polymer phases. The increase of the peak heights of the loss modulus, G'', is hereby linear with the filler volume fraction ϕ_F: $G''(T_g) = G''_0(T_g) + \alpha\phi_F$. Here, G''_0, is the value of the unfilled polymer. The

peak heights of the polymer phases in an unfilled blend in comparison to the peak heights of the pure polymers can be fitted by quadratic equations. The loss modulus of the blend, G''_{blend}, is then given by $G''_{\text{blend}} = \sum_i G''_{P,i}\left(a_i + b_i\phi_i + c_i\phi_i^2\right)$. $G''_{P,\,i}$ is the loss modulus of the i-th phase. Combining the effect of the filler with the blend effect yields

$$G''_{\text{blend}} = \sum_i \left(1 + \alpha_i \frac{\phi_{F,i}}{\phi_{F,i} + \phi_i}\right) G''_{P,i}\left(a_i + b_i\left(\phi_{F,i} + \phi_i\right) + c_i\left(\phi_{F,i} + \phi_i\right)^2\right) \quad (7)$$

This equation allows for the determination of the filler volume fractions, $\phi_{F,\,i}$, in the different phases when the peak heights of the loss modulus, G'', of filled and unfilled blends and the blend ratio are known. This method has already been applied to a variety of polymer blends [51–56]. The peak heights of the different polymer phases with and without filler are compared. There are two causes for the change in peak height of G'':

1. Linear increase of peak height with filler volume fraction
2. The change of phase volume fractions due to the filler in the different phases

The phase volume fraction has a nonlinear effect on the peak height of the loss modulus, G'', and is fitted by a quadratic function. In a blend the polymer with the lower glass transition has an overproportional peak height compared to its phase volume fraction. The polymer with the higher glass transition has an underproportional peak height and yields only a significant peak above a threshold value. At this threshold the polymer phase becomes continuous. Combining these two effects allows the determination of the filler distribution in the blend.

Besides the filling of the polymer phases, also amount and filling of the interphase can be obtained. Regarding the loss modulus, G'', the interphase can be seen as increased values between both glass transition peaks. For the calculation of interphase amount and filling, the interphase is assumed to consist of the same amount of both polymers, and all properties are the average of the properties of both polymers.

In NR/SBR blends, the SBR has the higher affinity to carbon black so that the SBR phase is higher filled than the NR phase. Therefore, the filling of the SBR phase is about twice as high as the filling of the NR phase. This is shown in Fig. 9 for the standard NR/SBR blend with blend ratios 70:30 and 55:45, respectively. In the batch mixing procedure, the NR is mixed with the carbon black first. Due to the higher affinity of the SBR, also in the batch compounds, the SBR phase is higher filled than the NR phase (Fig. 10). But as the filler needs to transfer from the NR to the SBR, the filling of the SBR phase is lower compared to the compounds mixed with the standard mixing procedure. Due to the increased carbon black transfer, the interphase contains also more filler.

In NR/BR blends the BR peak height is not increasing due to the filler, indicating very little amount of filler located in the BR phase. Accordingly, the NR phase is highly filled and contains most of the carbon black. In the batch mixing procedure,

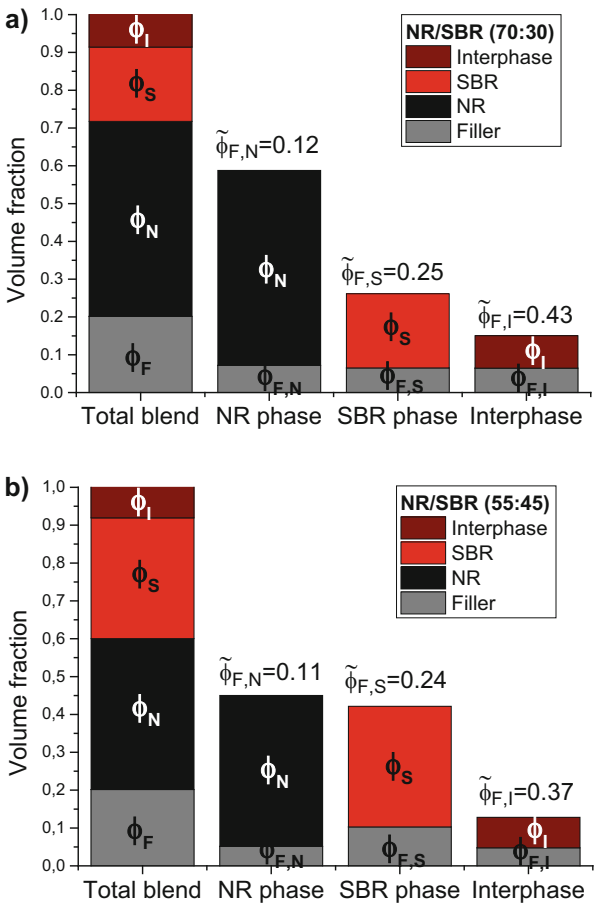

Fig. 9 Carbon black distribution in NR/SBR blend with blend ratios 70:30 (**a**) and 55:45 (**b**) both mixed according to standard procedure. The left column shows the phase proportion in the complete blend. The other columns show the amount of filler in the phases, $\phi_{F,i}$, and above the columns is given their filler volume fraction, $\tilde{\phi}_{F,i} = \phi_{F,i}/(\phi_i + \phi_{F,i})$ (from [49])

the carbon black is first mixed with the NR only. This leads to an even higher carbon black loading in the NR phase which is shown exemplary for the 70:30 blend ratio in Fig. 11. The lower filling of the BR phase can also be demonstrated by the TEM images depicted in Fig. 12. The bright BR phase contains clearly less of the dark carbon black particles than the darker NR phase.

The results concerning filler distribution in NR/BR blends, and the NR/SBR blends are summarized in Tables 2 and 3, respectively. Table 2 compares the proportions of the different phases consisting of carbon black $\tilde{\phi}_{F,i}$. In all NR/SBR blends, the SBR is higher filled than the NR phase. The BR phase in the NR/BR blends shows lower filling than the NR phase instead. The interphase in both blend systems is very highly filled. The carbon black affinity is found to be SBR $>$ NR $>$ BR. In Table 3 are shown the fractions of carbon black that are found in the different phases. For this not only the carbon black affinity but also the

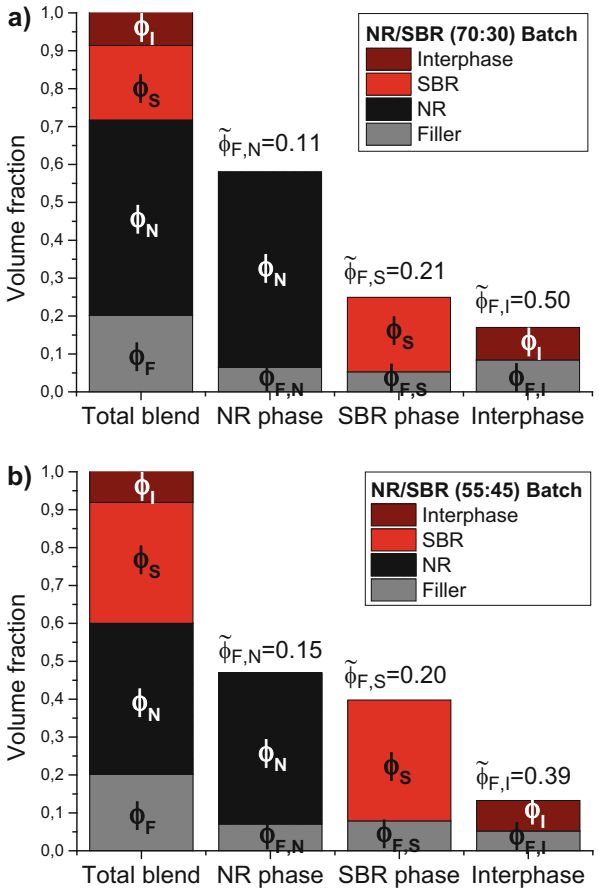

Fig. 10 Carbon black distribution in NR/SBR blend with blend ratios 70:30 (**a**) and 55:45 (**b**) both mixed according to batch mixing procedure. The left column shows the phase proportion in the complete blend. The other columns show the amount of filler in the phases, $\phi_{F,i}$, and above the columns is given their filler volume fraction, $\tilde{\phi}_{F,i} = \phi_{F,i}/(\phi_i + \phi_{F,i})$ (from [49])

size of the respective phase is decisive. So, the NR phase in the NR/SBR blends contains a substantial amount of the filler although its affinity to carbon black is low. On the contrary, the interphases, due to their small amounts, have only intermediate filler loadings, even when their affinity is very high.

In NR/BR/SBR blends, the filler is concentrated in the NR phase [57]. The thermally induced crystallization of the BR yields a second weak peak in the loss modulus, G'', which is located in the same temperature range as the NR glass transition peak [57]. This might hamper the calculation of the filler distribution in systems containing BR. The results of the filler distribution in the different blends are compared to previous findings which coincide for the NR/SBR blends fairly well [53, 54, 58–61]. These previous results were obtained by using inverse gas-liquid chromatography [58], phase-contrast optical microscopy [59, 62], combined static and dynamic modulus measurements [60], thermogravimetry on the rubber-filler gel [63], analysis of bound rubber [61], and earlier studies with the method presented in this chapter [53, 54, 64].

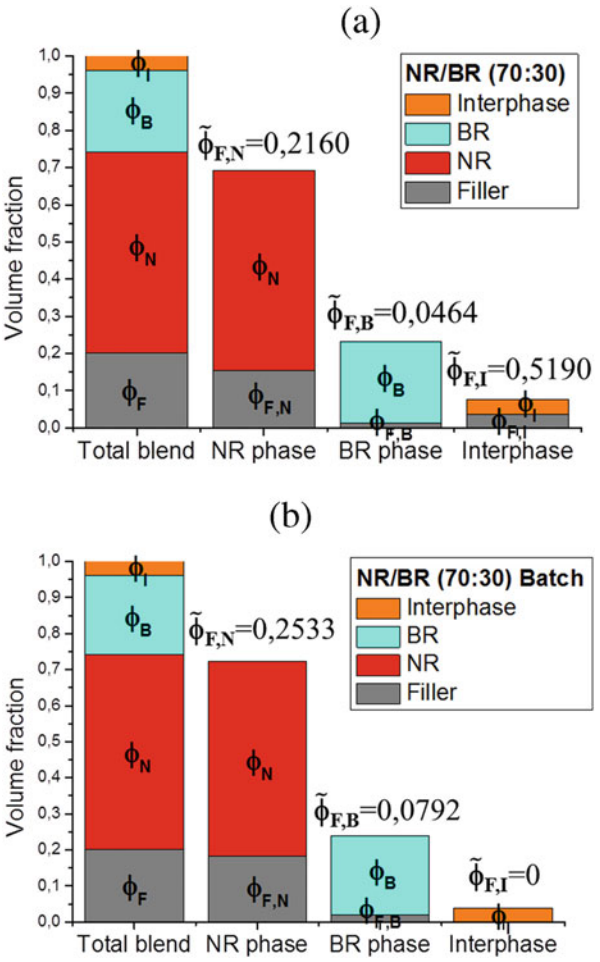

Fig. 11 Carbon black distribution in (70:30) NR/BR blends: (**a**) standard mixing procedure and (**b**) batch mixing procedure. The left column shows the phase proportion in the complete blend and the other columns show the amount of filler, $\phi_{F,i}$, in the phases. Above the columns their filler volume fraction, $\widetilde{\phi}_{F,i} = \phi_{F,i}/(\phi_i + \phi_{F,i})$, is shown (from [50])

5.2 *Fatigue Crack Growth Results*

It is well-known that the crack propagation speed in filler-reinforced rubber is much lower than that for unfilled rubbers [53, 65]. Therefore, carbon black filled rubber blends as listed in Table 1 are essential for truck tire tread compound to obtain a reasonable FCG behavior. The fatigue crack propagation behaviors of the investigated NR/BR blends and the NR/SBR blends are shown in Figs. 13 and 14, respectively. Due to the strengthening effect of strain-induced crystallization, pure

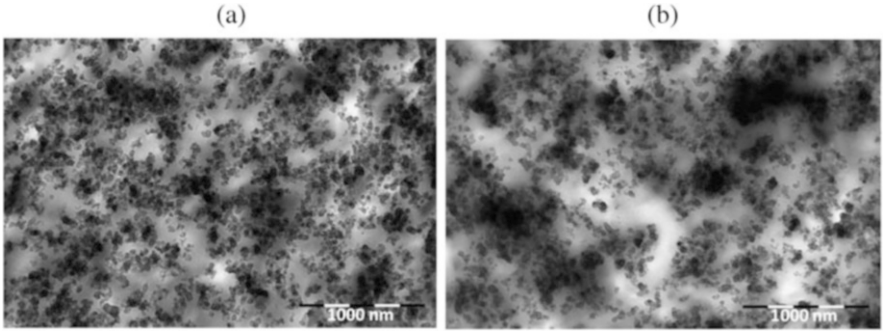

Fig. 12 TEM images of the (70:30) NR/BR blends: (**a**) standard mixing procedure and (**b**) batch mixing procedure (from [50])

Table 2 Proportion of the different phases consisting of carbon black $\widetilde{\phi}_{F,i} = \phi_{F,i}/(\phi_i + \phi_{F,i})$. ϕ_i and $\phi_{F,\,i}$ are the volume fractions of polymer and filler, respectively, that are located in phase i

Compound	Filler volume fraction			
	$\widetilde{\phi}_{F,N}$	$\widetilde{\phi}_{F,B}$	$\widetilde{\phi}_{F,S}$	$\widetilde{\phi}_{F,I}$
N85B15	0.21	0	–	0.70
N70B30	0.22	0.05	–	0.52
N70B30 batch	0.25	0.08	–	0
N55B45	0.20	0.11	–	0.60
N55B45 batch	0.26	0.14	–	0.06
N85S15	0.11	–	0.50	0.34
N70S30	0.12	–	0.25	0.43
N70S30 batch	0.11	–	0.21	0.50
N55S45	0.11	–	0.24	0.37
N55S45 batch	0.15	–	0.20	0.39

Table 3 Fraction $\phi_{F,\,i}/\phi_F$ of carbon black that is found in the different phases [%]. $\phi_{F,\,i}$ and ϕ_F are the volume fractions of filler that are located in phase i and in all phases, respectively

Compound	$\frac{\phi_{F,N}}{\phi_F}$	$\frac{\phi_{F,B}}{\phi_F}$	$\frac{\phi_{F,S}}{\phi_F}$	$\frac{\phi_{F,I}}{\phi_F}$
N85B15	90	0	–	10
N70B30	74	5	–	10
N70B30 batch	91	9	–	0
N55B45	51	20	–	29
N55B45 batch	72	26	–	1
N85S15	41	–	41	19
N70S30	36	–	32	32
N70S30 batch	32	–	26	42
N55S45	26	–	51	24
N55S45 batch	35	–	39	26

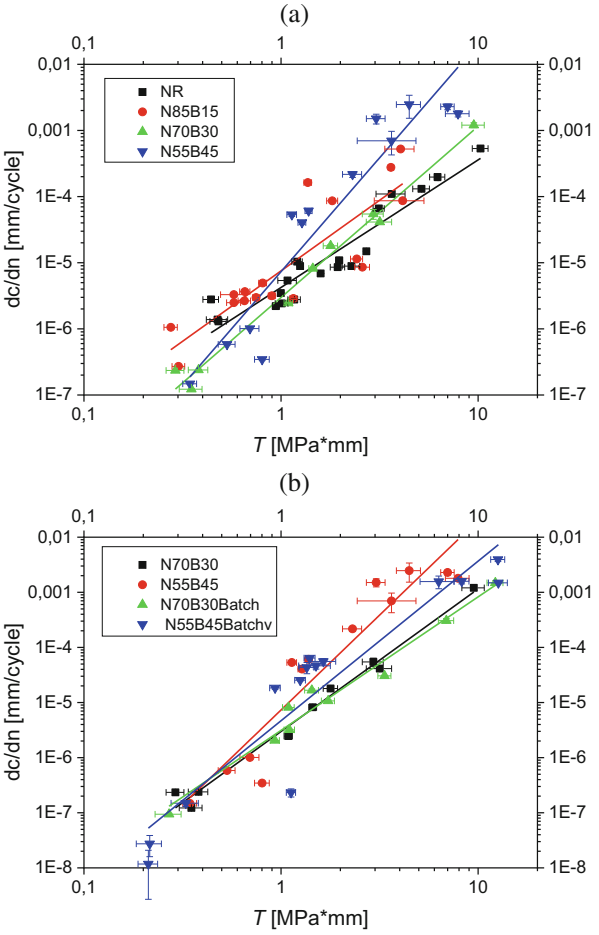

Fig. 13 Crack growth rate, *dc/dn*, vs. tearing energy, *T*: for NR/BR blends obtained with standard mixing procedure (**a**) and for NR/BR blends obtained with batch mixing procedure in comparison to the standard mixing procedure (**b**) (from [49])

NR is found to have the lowest crack propagation rates in comparison to NR blends with BR and/or SBR [66]. Increasing the SBR content leads to higher crack propagation rates for all loading intensities quantified by the tearing energy *T*. The steep slope of the N55S45Batch compound can be explained by the very low filler dispersion of this compound, which is by far lower than the other compounds. Increasing the BR content does not change the crack propagation at low tearing energies. However, for high tearing energies, the FCG rate, *dc/dn*, is strongly increasing with BR content. The crack propagation is also influenced by the mixing technique. This can be seen in the N70B30Batch compound that has lower FCG compared to the N70B30 compound mixed with the standard mixing procedure (see Fig. 13b). The higher FCG resistance of the batch is attributed to the higher filled NR phase which leads to more strain-induced crystallization of the NR at the same strain.

The Chip & Cut effect of truck tires denotes loss of tire tread material when trucks are driving on rough roads [67]. The Chip & Cut effect requires harsh conditions and

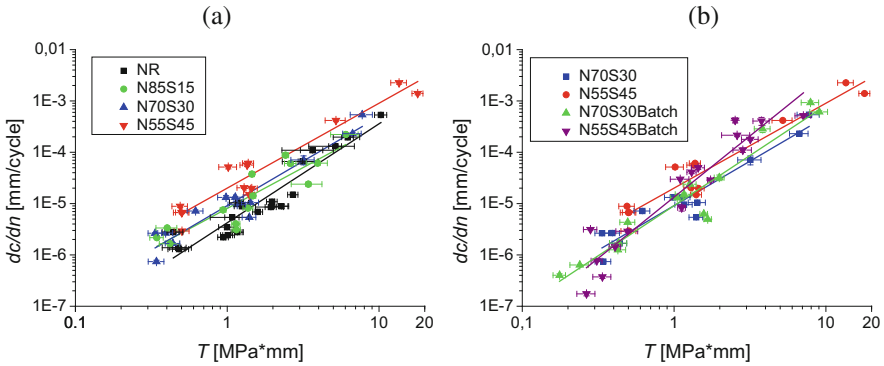

Fig. 14 Crack growth rate, *dc/dn*, vs. tearing energy, *T*: for NR/SBR blends obtained with standard mixing procedure (**a**) and for NR/SBR blends obtained with batch mixing procedure in comparison to standard mixing procedure (**b**) (from [48])

appears firstly at high tearing energy. The rating of the Chip & Cut performance of truck tire treads is based on the wear appearance after testing. These have been investigated in [68] for four selected compounds. The ranking of Chip & Cut resistance is found as NR > N55S45 > N55B23S23 > N55B45, which correlates with the ranking of the cut growth rate at high tearing energy. In particular, the crack propagation rates of N55B45 exhibit the largest values. This is probably the reason for the most pronounced Chip & Cut effect for N55B45. The results also correlate with the instrumented Chip & Cut test [69].

6 Conclusions

For the crack growth rate in viscoelastic rubber materials not the tearing energy is the decisive energy, but the part of the tearing energy that reaches the process zone. The process zone in close vicinity of the crack tip. The dissipative energy loss around the crack tip is determined with the J-integral, which is increasing from very low values for small integration radii around the crack tip toward a plateau for larger radii. The plateau value coincides roughly to the global value of tearing energy obtained with Eq. (3). The increase from low values into the plateau corresponds to the viscoelastic energy losses that do not directly affect crack growth.

Fatigue crack growth measurements at filled rubber blends show that the crack growth rate is lowest for the strain-crystallizing NR. Increasing the SBR portion in a NR/SBR blend leads to an increased crack growth for all tearing energies, and increasing the BR portion in NR/BR blends yields strongly increased crack growth for higher tearing energies. This could be connected to the Chip & Cut behavior measured in truck tire tests.

The crack growth rate of the investigated filled rubber blends is only slightly affected by the blend morphology and filler distribution in the blend, which can be manipulated, e.g., by the mixing procedure. Through a comparison of dynamical spectra from unfilled and filled blends, the filler distribution can be calculated. This calculation yields high filler loadings in the SBR phase and the interphase in NR/SBR blends, but low filler loading in the BR phase in NR/BR blends.

Acknowledgments We would like to thank our project partners Leibniz-Institut für Polymerforschung e.V. and Continental Reifen Deutschland GmbH for the very good cooperation. Continental is appreciated for mixing the compounds in industrial scale. The Deutsche Forschungsgemeinschaft (DFG) is appreciated for financial support (grant KL 1409/9-1).

References

1. Trabelsi S, Albouy P-A, Rault J (2002) Stress-induced crystallization around a crack tip in NR. Macromolecules 35:10054–10061
2. Vilgis TA, Heinrich G, Klüppel M (2009) Reinforcement of polymer nano-composites. Cambridge University Press, Cambridge
3. Grosch KA (1989) Visko-elastische Eigenschaften von Gummimischungen und deren Einfluß auf das Verhalten von Reifen. Kaut Gummi Kunst 42:745–751
4. Röthemeyer F, Sommer F (2001) Kautschuktechnologie. Carl Hanser Verlag, München
5. Huneau B, Masquelier I, Marco Y, Le Saux V, Noizet S, Schiel C, Charrier P (2016) Fatigue crack initiation in a carbon black-filled natural rubber. Rubber Chem Technol 89:126–141
6. Ludwig M, Alshuth T, El Yaagoubi H, Juhre D (2015) Lifetime prediction of elastomers based on statistical occurrence of material defects. In: Marvalová B, Petríková I (eds) Constitutive models for rubber IX. Taylor & Francis, London, pp 445–448
7. Griffith AA (1920) The phenomena of rupture and flow in solids. Philos Trans R Soc Lond Ser A 221:163–198
8. Anderson TL (1995) Fracture mechanics. CRC Press, Boca Raton
9. Eisele U (1978) Zum Einfluss der Mikrostruktur auf die Weiterreißenergie von Synthesekautschuken. Gummi Asbest Kunst 31:724–730
10. Liu C, Dong B, Zhang L-Q, Zheng Q, Wu YP (2015) Influence of strain amplification near crack tip on the fracture resistance of carbon black-filled SBR. Rubber Chem Technol 88:276–288
11. Bhowmick AK, Gent AN, Pulford CTR (1983) Tear strength of elastomers under threshold conditions. Rubber Chem Technol 56:226–232
12. Persson BNJ, Brener EA (2005) Crack propagation in viscoelastic solids. Phys Rev E 71:036123
13. Persson BNJ, Albohr O, Heinrich G, Ueba H (2005) Crack propagation in rubber-like materials. J Phys Condens Matter 17:R1071
14. Heinrich G, Klüppel M, Vilgis T, Horst T (2012) Wenn Gummi zu Bruch geht. Phys J 11:39–44
15. Holownia BP (1975) Effect of carbon black on Poisson's ratio of elastomers. Rubber Chem Technol 48:246–253
16. Kugler HP, Stacer RG, Steimle C (1990) Direct measurement of poisson's ratio in elastomers. Rubber Chem Technol 63:473–487
17. Rivlin RS, Thomas AG (1953) Rupture of rubber. I. Characteristic energy for tearing. J Polym Sci 10:291–318
18. Clapson BE, Lake GJ (1971) Truck tire groove cracking – theory and practice. Rubber Chem Technol 44:1186–1202

19. Thomas AG (1994) The development of fracture mechanics of elastomers. Rubber Chem Technol 67:50–366
20. Rice JR (1968) A path independent integral and the approximate analysis of strain concentration by notches and cracks. J Appl Mech 35:379–386
21. Cherepanov GP (1967) Crack propagation in continuous media. J Appl Math Mech 31:503–512
22. Holzapfel GA (2001) Nonlinear solid mechanics. Wiley, Chichester
23. Maugin GA (1995) Material forces: concepts and applications. Appl Mech Rev 48:213–245
24. Eshelby JD (1975) The elastic energy-momentum tensor. J Elast 5:321–335
25. Freund LB (1998) Dynamic fracture mechanics. Cambridge University Press, Cambridge
26. Zehnder AT (2012) Fracture mechanics. Lecture notes in applied and computational mechanics, vol 62, pp 33–54
27. Horst T, Heinrich G, Schneider M, Schulze A, Rennert M (2013) Linking mesoscopic and macroscopic aspects of crack propagation in elastomers. Lecture notes in applied and computational mechanics, vol 70, pp 129–165
28. Gent AN, Lindley PB, Thomas AG (1964) Cut growth and fatigue of rubbers. I. The relationship between cut growth and fatigue. J Appl Polym Sci 8:455–466
29. Robertson CG, Stoček R, Kipscholl R, Mars WV (2019) Characterizing the intrinsic strength (fatigue threshold) of natural rubber/butadiene rubber blends. Tire Sci Technol 47:78–82
30. Lake GJ, Thomas AG (1967) Physics of failure in rubber. Kaut Gummi Kunst 20:211–217
31. Paris PC, Gomez MP, Anderson WE (1961) A rational analytic theory of failure. Trend Eng 13:9–14
32. Paris PC, Erdogan F (1963) A critical analysis of crack propagation laws. J Basic Eng 85:528–533
33. Irwin GR (1957) Analysis of stresses and strain near the end of a crack traversing a plate. Trans ASME Ser E J Appl Mech 24:361–364
34. de Gennes PG (1996) Soft adhesives. Langmuir 12:4497–4500
35. Rubinstein M, Colby RH (2003) Polymer physics. Oxford University Press, New York
36. Klüppel M (2009) Evaluation of viscoelastic master curves of filled elastomers and application to fracture mechanics. J Phys Condens Matter 21:035104
37. Le Gal A, Klüppel M (2008) Investigation and modeling of rubber stationary friction on rough surfaces. J Phys Condens Matter 20:015007
38. Le Gal A, Klüppel M (2006) Investigation and modeling of adhesion friction on rough surfaces. Kaut Gummi Kunst 59:308–315
39. Williams ML, Ferry JD (1953) Second approximation calculations of mechanical and electrical relaxation and retardation distributions. J Polym Sci 11:169–175
40. Wunde M, Klüppel M (2018) Viscoelastic response during crack propagation of unfilled and filled SBR. Rubber Chem Technol 91(668):682
41. Lake GJ, Lindley PB (1964) Ozone cracking, flex cracking and fatigue of rubber. Part one: cut growth mechanisms and how they result in fatigue failure. Rubber J 146:24–30
42. Lake GJ, Lindley PB (1964) Ozone cracking, flex cracking and fatigue of rubber. Part two: technological aspects. Rubber J 146:30–36
43. Gent AN (1996) Adhesion and strength of viscoelastic solids. Is there a relationship between adhesion and bulk properties. Langmuir 12:4492–4496
44. Gent AN, Lai S-M (1994) Interfacial bonding, energy dissipation, and adhesion. J Polym Sci B Polym Phys 32:1543–1555
45. Ludwig M (2017) Entwicklung eines Lebensdauer-Vorhersagekonzepts für Elastomerwerkstoffe unter Berücksichtigung der Fehlstellenstatistik. PhD thesis, Hannover, Germany
46. Wunde M, Plagge J, Klüppel M (2019) The role of stress softening in crack propagation of filler reinforced elastomers as evaluated by the J-integral. Eng Fract Mech 214:520–533
47. Plagge J, Klüppel M (2017) A physically based model of stress softening and hysteresis of filled rubber including rate-and temperature dependency. Int J Plast 89:173–196
48. Klüppel M, Schramm J (2000) A generalized tube model of rubber elasticity and stress softening of filler reinforced elastomer systems. Macromol Theory Simul 9:742–754

49. Wunde M, Klüppel M (2017) Impact of mixing procedure on phase morphology and fracture mechanical properties of carbon black-filled NR/SBR blends. Contin Mech Thermodyn 29:1135–1148
50. Wunde M, Klüppel M (2016) Influence of phase morphology and filler distribution in NR/BR and NR/SBR blends on fracture mechanical properties. Rubber Chem Technol 89:588–607
51. Meier JG, Klüppel M, Geisler H, Schuster RH (2005) Kieselsäuregefüllte Elastomerblends durch Masterbatchtechnologie. Kaut Gummi Kunst 58:587
52. Meier JF, Klüppel M, Schuster RH (2005) Steuerung der physikalischen Eigenschaften von Elastomeren. Kaut Gummi Kunst 58:82
53. Lorenz H, Steinhauser D, Klüppel M (2013) Morphology and micro-mechanics of filled elastomer blends: impact on dynamic crack propagation. Lecture notes in applied and computational mechanics, vol 70, pp 81–128
54. Klüppel M, Schuster RH, Schaper J (1999) Carbon black distribution in rubber blends: a dynamic-mechanical analysis. Rubber Chem Technol 72:91
55. Klüppel M, Schuster RH, Schaper J (1998) Dynamischer Glasübergang in füllstoffverstärkten Kautschukblends. GAK Gummi Fasern Kunst 51:508
56. Schuster RH, Meier JF, Klüppel M (2000) The role of interphase in filler partition in rubber blends. Kaut Gummi Kunst 53:663
57. Wunde M, Klüppel M (2020) Effect of filler and blending with SBR and NR on thermally induced crystallization of high-cis BR as evaluated by dynamic mechanical analysis. Express Polym Lett 14(3):261–271
58. Schuster RH, Issel HM, Peterseim V (1996) Selective interactions in elastomers, a base for compatibility and polymer-filler interactions. Rubber Chem Technol 69:769
59. Hess WM, Scott CE, Callan JE (1967) Carbon black distribution in elastomer blends. Rubber Chem Technol 40:371–383
60. Ayala JA, Hess WM, Kistler FD, Joyce GA (1991) Carbon-black – elastomer interaction. Rubber Chem Technol 64:19–39
61. Callan JE, Hess WM, Scott CE (1971) Elastomer blends. Compatibility and relative response to fillers. Rubber Chem Technol 44:814
62. Le HH, Ilisch S, Kasaliwal GR, Radusch H-J (2008) Filler phase distribution in rubber blends characterized by thermogravimetric analysis of the rubber-filler gel. Rubber Chem Technol 81:767–781
63. Cotton GR, Murphy LJ (1988) Mixing of carbon black with rubber. Part 5. Analysis of BR/SBR blends. Kaut Gummi Kunst 41:54–58
64. Meier JF, Klüppel M, Schuster RH (2005) Steuerung der physikalischen Eigenschaften von Elastomeren. Kaut Gummi Kunst 58:82–89
65. Reincke K, Grellmann W, Klüppel M (2009) Investigations of fracture mechanical properties of filler-reinforced styrene-butadiene elastomers. Kaut Gummi Kunst 62:246–251
66. Hamed GR, Kim HJ, Gent AN (1996) Cut growth in vulkanizates of natural rubber, cis-polybutadiene, and a 50/50 blend during single and repeated extension. Rubber Chem Technol 69:807
67. Stocek R, Kipscholl R, Euchler E, Heinrich G (2014) Study of the relationship between fatigue crack growth and dynamic chip & cut behavior of reinforced rubber materials. Kaut Gummi Kunst 67(4):26–29
68. Wunde M, Schulze A, Vatterott C, Tschimmel J, Lacayo-Pineda J, Heinrich G, Klüppel M (2019) Verbesserung der Laborvorhersagen zum Risswachstum und Verschleiß von LKW-Reifenlaufflächen. Kaut Gummi Kunst 72(8):72–78
69. Stocek R, Heinrich G, Schulze A, Wunde M, Klüppel M, Vatterott C, Tschimmel J, Lacayo-Pineda J, Kipscholl R (2020) Chip & cut wear of truck tire treads: comparison between laboratory and real tire testing. Kaut Gummi Kunst 73(6):51–55
70. Robertson CG, Stoček R, Mars WV (2021) The fatigue threshold of rubber and its characterization using the cutting method. In: Heinrich G, Stoček R, Kipscholl R (eds) Fatigue crack growth in rubber materials: experiments and modelling. Springer, Heidelberg. https://doi.org/10.1007/12_2020_71